Supporting Information for

Inert Is Not Inactive: Origin of Carbon Dioxide Electroreduction Activity over Carbon Current Collector-based Electrode

Minyang Dai, [#a] Wenpeng Ni, [#a] Zhouliangzi Zeng, [a] Wei Zhang, [a] Yan Zhang, [a] Shuangyin Wang[b], and Shiguo Zhang*,[a]

[a] College of Materials Science and Engineering, Key Laboratory for Advanced Catalytic Engineering Research Center of the Ministry of Education, Hunan University, Changsha 410028, China

[b] College of Chemistry and Chemical Engineering, Provincial Hunan Key Laboratory for Graphene, State Key Laboratory of Chem/Bio-Sensing, Hunan University, Changsha 410028, China

[#] These authors contributed equally to this work.

Corresponding author:

Prof. Shiguo Zhang (zhangsg@hnu.edu.cn)

Supporting Information Text

Chemicals and materials

1,2,4,5-tetramethylimidazole, acetonitrile (water≤50 ppm, 99.9%) tetrabutylammonium hexafluorophosphate ([TBA]PF_6, purity >99%) were purchased from Adamas. 1-Butyl-3-methylimidazolium hexafluorophosphate ([BMIm]PF_6, purity >99%), 1-Butyl-2,3-methylimidazolium hexafluorophosphate ([BMMIm]PF_6, purity >99%) and 1-Butyl-2,3-methylimidazolium acetate ([BMMIm]OAc, purity >99%) was provided by the Centre of Green Chemistry and Catalysis, Lanzhou Institute of Chemical Physics, Chinese Academy of Sciences. Ti fiber paper was purchased Sinero and the model number is STi025.The manufacturer of the carbon paper we used is Toray, and the model number is TGP-H-060, without any hydrophobic treatment.

Methods

Synthesis of g-C_3N_4: The g-C_3N_4 was prepared by calcinating melamine in a muffle furnace at 500 ^oC for 6 h with a heating rate of 2 ^oC/min.

Synthesis of NCNT: CNT was washed by 4 M HNO_3 at 80 ^oC before use. Then we mixed 0.1g CNT with 1g melamine and pyrolyzed at 800 ^oC for an hour to obtain NCNT.

Synthesis of oxidation-treated KB: The KBO-450 was prepared by calcinating KB powders in a muffle furnace at 450 ^oC for 2 h. As for KBO-600, the same method was accepted excluding the temperature is 600 ^oC.

Acid-treated KB: Acid-treated KB was prepared by subjecting 100 mg of KB to ultrasonication in 25 mL of 98% H_2SO_4 for 20 min. Then the homogenous suspension was magnetically stirred and 75 mL of 30% of H_2O_2 was added for 4 h. Oxidized KB were collected by centrifugation at 7000 rpm, rinsed thoroughly with de-ionic water, and dried in a vacuum oven at 60 ^oC overnight.

Synthesis of BM_4ImPF_6: 1,2,4,5-tetramethyl-imidazole (0.01 mol) was reacted with iodobutane (0.015 mol), neat, at 40 °C for 12 hours. The solution was allowed to cool to room temperature, and a yellow solid was obtained. The solid was repeatedly washed with diethyl ether (5 x 20 mL), then recrystallized from acetone to obtain transparent crystals of 1-butyl-2,3,4,5-tetramethylimidaozlium iodide. A portion of the iodide salt (0.005 mol) was reacted with silver tetrafluoroborate (0.005 mol) in 10 mL of water. The mixture was stirred for 18 hours at room temperature in the dark. The yellow precipitate (AgI) was removed via centrifugation (6000 rpm, 25 minutes). The aqueous phase was

transferred to a separating funnel and extracted with 50 mL of dichloromethane. The organic extracts were combined and dried over anhydrous Na_2SO_4. Removal of the solvents under reduced pressure at 40 °C gave the product as a colorless solid.

Electrochemical Experiments

In this study, all the electrochemical measurements were obtained using a Biological electrochemical workstation and a costume-made three-electrode cell. The working electrode was commercial carbon fiber paper or Ti fiber paper (0.5×0.5 cm^{-2}). We washed them with acetone, de-ionic water, and ethanol three times before testing. Ag/Ag^+ reference electrode (0.1 M $AgNO_3$, 0.1 M $TBAPF_6$, CH_3CN) was used as a reference electrode and Pt mesh as the counter electrode, respectively. The catholyte was ionic liquid/MeCN/H_2O and the anolyte was 0.5 M H_2SO_4 (25 mL for each compartment). A bipolar membrane (BPM) was used to separate two compartments of the cell. Prior to all electrochemical measurements, the ionic liquid salts were dried in a vacuum for 5 h at 70 ^oC. The catholyte was supposed to be bubbled with CO_2 for at least 30 minutes (30 sccm, calibrated by mass flow controller) before testing. For CO_2 reduction experiments, LSV measurement was conducted in gas-saturated electrolytes at the scan rate of 10 mV s^{-1}. Constant potential electrolysis was carried out at various potentials for 25 min to analyze the corresponding products. The gaseous products were collected and analyzed using SHIMADZU GC 2014 gas chromatograph equipped with a thermal conductivity detector (TCD) and a flame ionization detector (FID). After the quantification, the FE and current density toward each product were calculated as follows:

$$FE(\%) = \frac{\text{amount of the product} \times n \times F}{C}$$

$$jCO = FECO \times jtotal$$
$$jH2 = FEH2 \times jtotal$$

where n is number of moles of electrons to participate in the Faradaic reaction, F is the Faraday constant (96485 C mol^{-1}), and C is the amount of charge passed through the working electrode.

Tafel slopes were calculated corresponding to the linear sweep voltammetry plots, which is derived from the total current density and faradaic efficiency of CO production.

$$\eta = E0 - E = -b\log j0 + b\log jco$$

$$b = 2.3RT/aF$$

where E is the applied potential; Eo is the equilibrium potential for the CO_2 /CO couple; η is the overpotential for the CO_2 /CO couple; a is the transfer coefficient; b is the Tafel slope; jo is the exchange current density; and j_{CO} is the CO current density.

Characterization

Ultra-pure purification system (Master-S15Q, Hitech Instruments Co. Ltd., Shanghai, China) was used to produce 18.2 MΩ/cm water in all experiments. The phase identification was characterized by powder X-ray diffraction using Cu Kα radiation (RikaguMiniFlex600). X-ray photoelectron spectrum (XPS) data was collected by ECSALAB250Xi spectrometer with an Al Kα X-ray radiation for excitation, and the binding energy was corrected by C 1s value of 284.6 eV. The morphologies of the samples were determined by Field emission scanning electron microscopy (SEM, Hitachi S-4800) and high-resolution transmission electron microscopy (HRTEM, Titan G2 60-300) equipped with energy dispersive X-ray spectroscopy (EDS) mapping. Raman spectra were obtained by a DXRI Raman Microscope (Thermo Fisher) using a 532 nm laser as the light source. In situ ATR-FTIR experiment was performed using Fourier transform infrared spectrometer (Nicolet iS50), coupling with a three-electrode electrochemical cell (SPEC-I, Yuanfang Co. Ltd., Shanghai, China). A thin layer of Au film was coated on Si prism for loading electrocatalysts as working electrode, Ag/Ag^+ and Pt wire were used as the reference and counter electrodes, respectively. The nuclear magnetic resonance (^{1}H-NMR) measurements were conducted on a Bruker spectrometer (400 MHz) in d-DMSO. The HRMS spectra of electrolytes was obtained via electro-spray ionization (ESI) by Thermo Scientific QTOF6550 and the mass spectra of products was collected on SHIMADZU GCMS-QP202. The ion chromatography of electrolytes was obtained on Thermo Scientific AQUION RFIC for detecting F^-. The water content of electrolytes was determined by Karl Fischer titrations experiments on KF-Coulom cell D831.

Calculation method

The DFT calculations were carried out using the Vienna Ab-initio Simulation Package (VASP)[1-2] with the frozen-core all-electron projector-augment-wave (PAW)[3-4] method. The Perdew-Burke-Ernzerhof (PBE)[5] of generalized gradient approximation (GGA) was adopted to describe the exchange and correlation potential. The cutoff energy for the plane-wave basis set was set to 450 eV. A mono-layer 4×4 graphene supercell was used, and a vacuum region of 20 Å above it was used to ensure the decoupling between neighboring systems. The F-doped graphene was built based on a pure graphene

supercell. The geometry optimizations were performed until the forces on each ion were reduced below 0.01 eV/Å, and a 5×5×1 Monkhorst-Pack k-point[6] sampling of the Brillouin zone was used.

The adsorption energy(ΔEads), is calculated using the expression

$\Delta E_{ads} = E_{molecule+surface} - E_{surface} - E_{molecule}$

where $E_{surface}$ is the energy of the pure graphene or F-doped graphene, Emolecule represents the energy of the F or OH, and $E_{molecule+surface}$ represents the total energy of the adsorbed system.

The Gibbs free energy (ΔG) is calculated as

$\Delta G = E_{DFT} + \Delta E_{ZPE} - T\Delta S$

ΔE_{ZPE} is the difference corresponding to the zero point energy between the adsorbed molecule and molecule in the gas phase and ΔS is one molecule entropy between the absorbed state and gas phase. E_{DFT} is the total energy of the DFT calculated system. The authors extend their gratitude to Haijiao Xie from Shiyanjia Lab (www.shiyanjia.com) for providing invaluable assistance with the calculations.

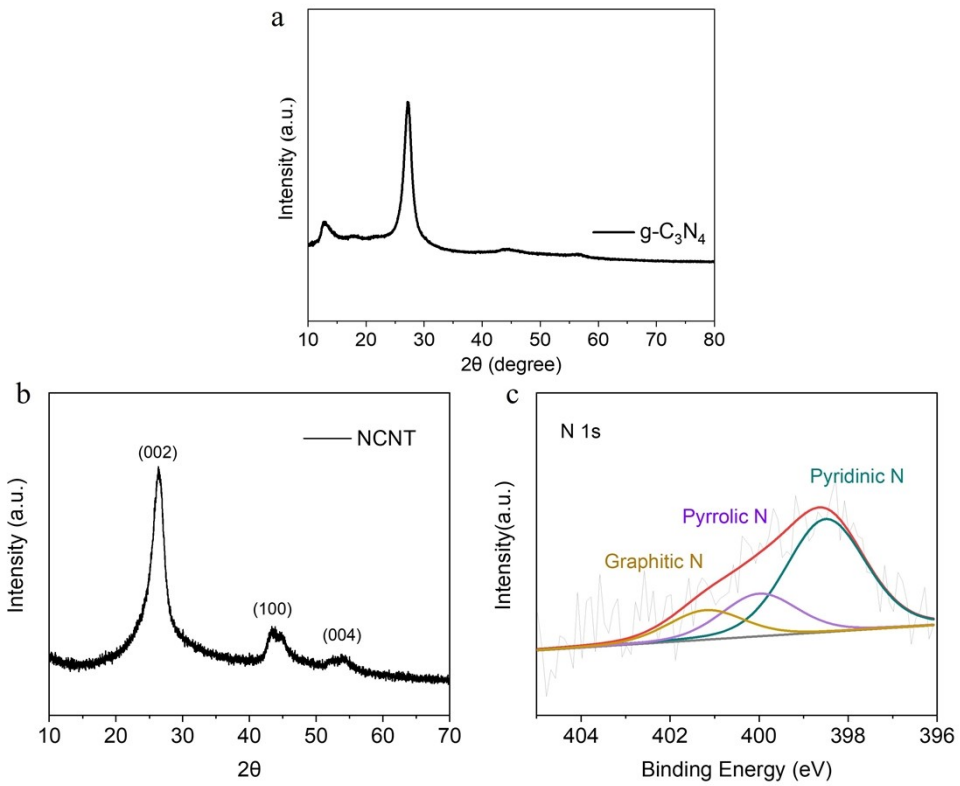

Figure S1. XRD pattern of (a) g-C_3N_4 and (b) NCNT. High-resolution N1s spectra of (c) NCNT.

As shown in **Figure S1a**, two characteristic diffraction peaks for g-C_3N_4 appear at 2θ = 12.9 and 27.5 °, corresponding to (1 0 0) and (0 0 2) planes. The strong peak at 27.5° , featuring an interlayer of 0.323 nm, is a result of the stacking of the conjugated aromatic system, while the weak peak at 12.9° is indicative of the in-plane structural packing motif. As for NCNT, the XRD analysis reveals three discernible peaks at 2θ=26.3°, 43°, and 53°, assigning to the (002), (100), and (004) planes, respectively (**Figure S1b**). The total content of the N atom is 0.51at% detected by XPS analysis. In **Figure S1c**, the high-resolution N 1 s XPS spectra of NCNT have been deconvoluted into three peaks corresponding to pyridinic N (398.5 eV), pyrrolic N (400.0 eV), and graphitic N (401.2 eV), among which the pyridinic N was the dominant N species with the percentage of 62%.

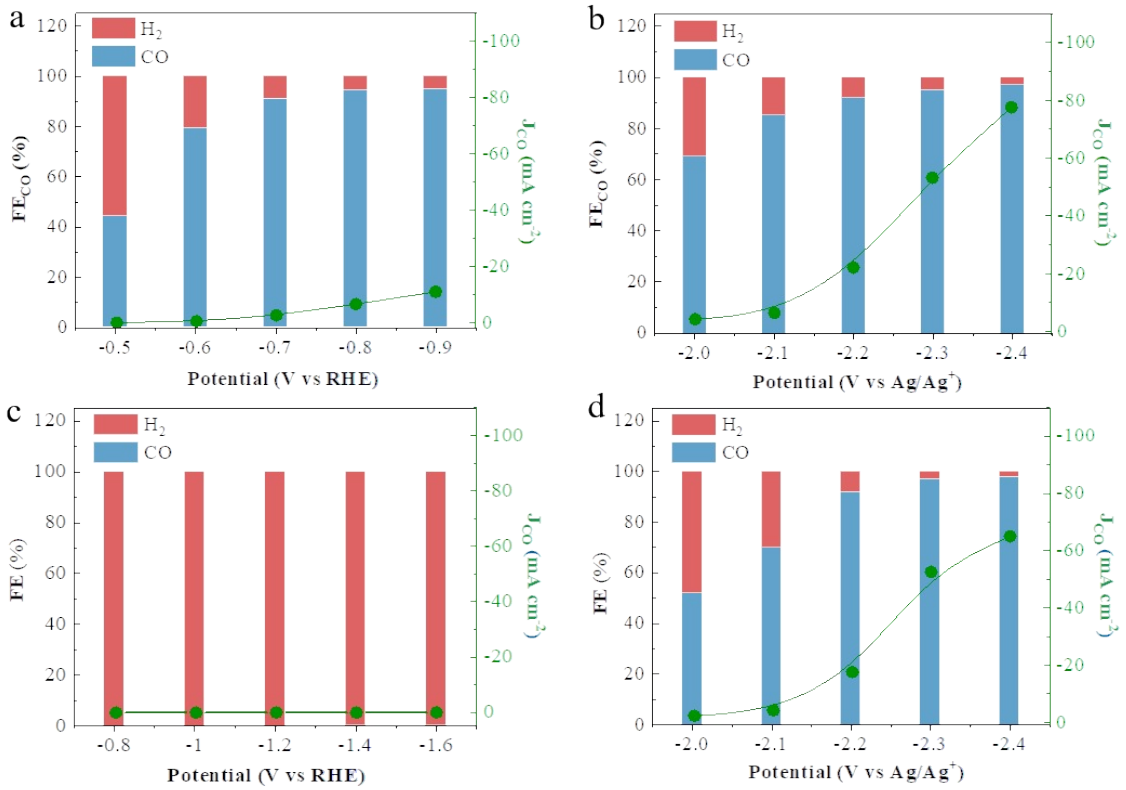

Figure S2. Faradaic efficiency and partial current density of CO for (a) NCNT in 0.1 M $KHCO_3$, (b) NCNT in $TBAPF_6/CH_3CN/H_2O$, (c) g-C_3N_4 in 0.1 M $KHCO_3$, (d) g-C_3N_4 in $TBAPF_6/CH_3CN/H_2O$.

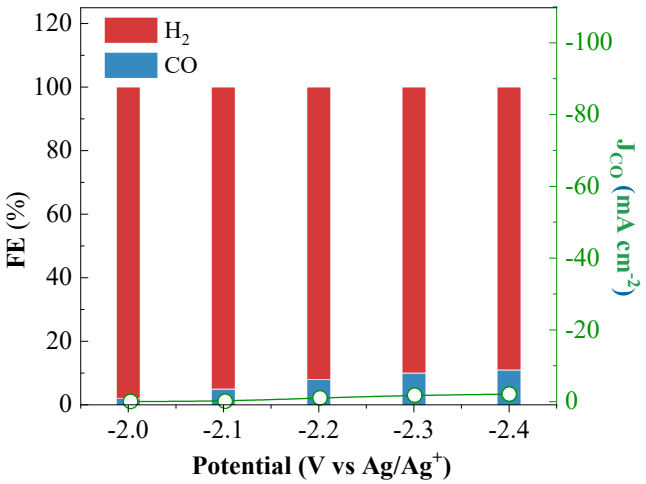

Figure S3. Faradaic efficiency and partial current density of CO for Ti paper in $TBAPF_6/CH_3CN/H_2O$.

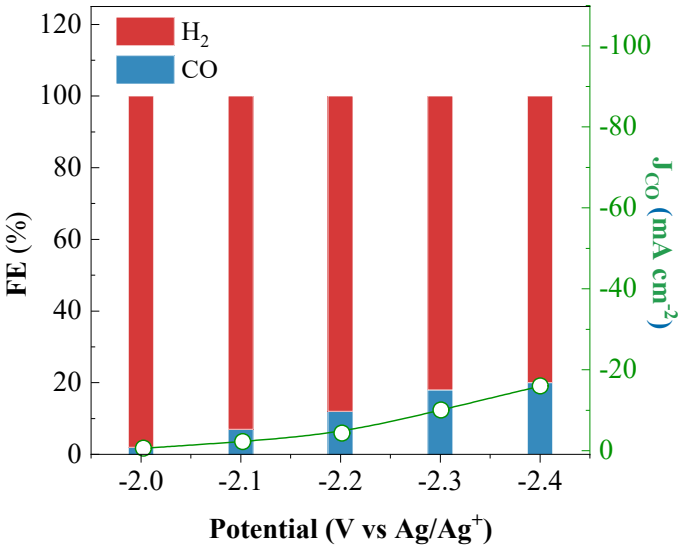

Figure S4. Faradaic efficiency of H_2 and CO for g-C_3N_4/Ti in TBAPF_6/CH_3CN/H_2O.

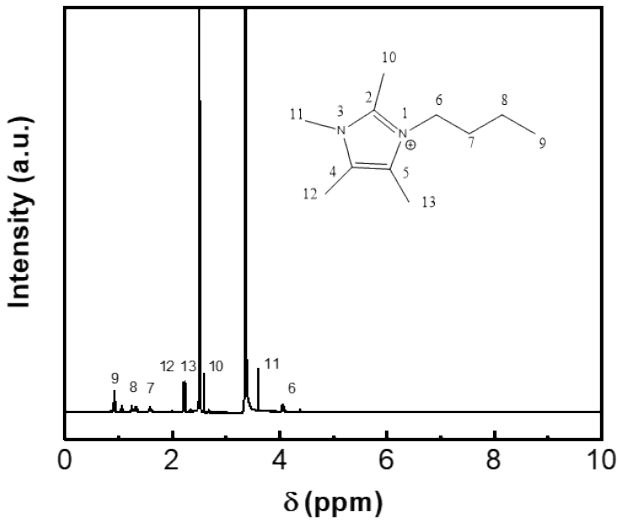

Figure S5. H-NMR spectra for BM_4ImPF_6.

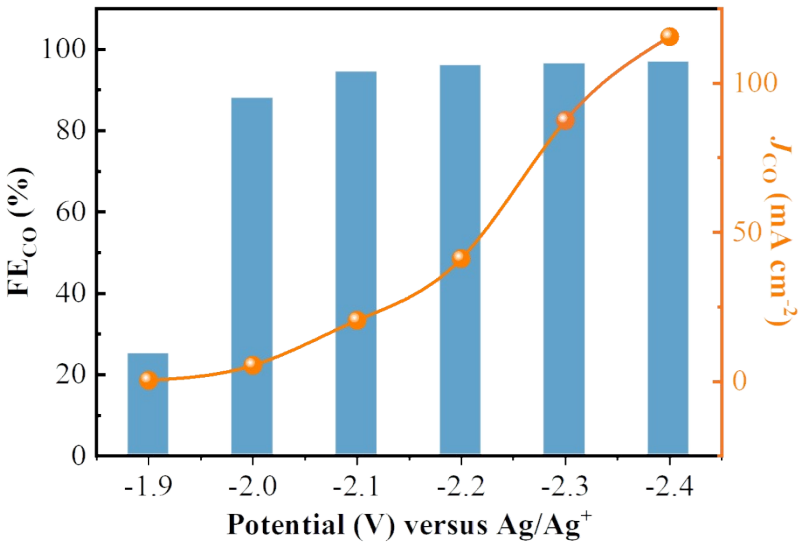

Figure S6. Electrochemical CRR performance of CP in $BMMImBF_4$/MeCN/H_2O electrolytes.

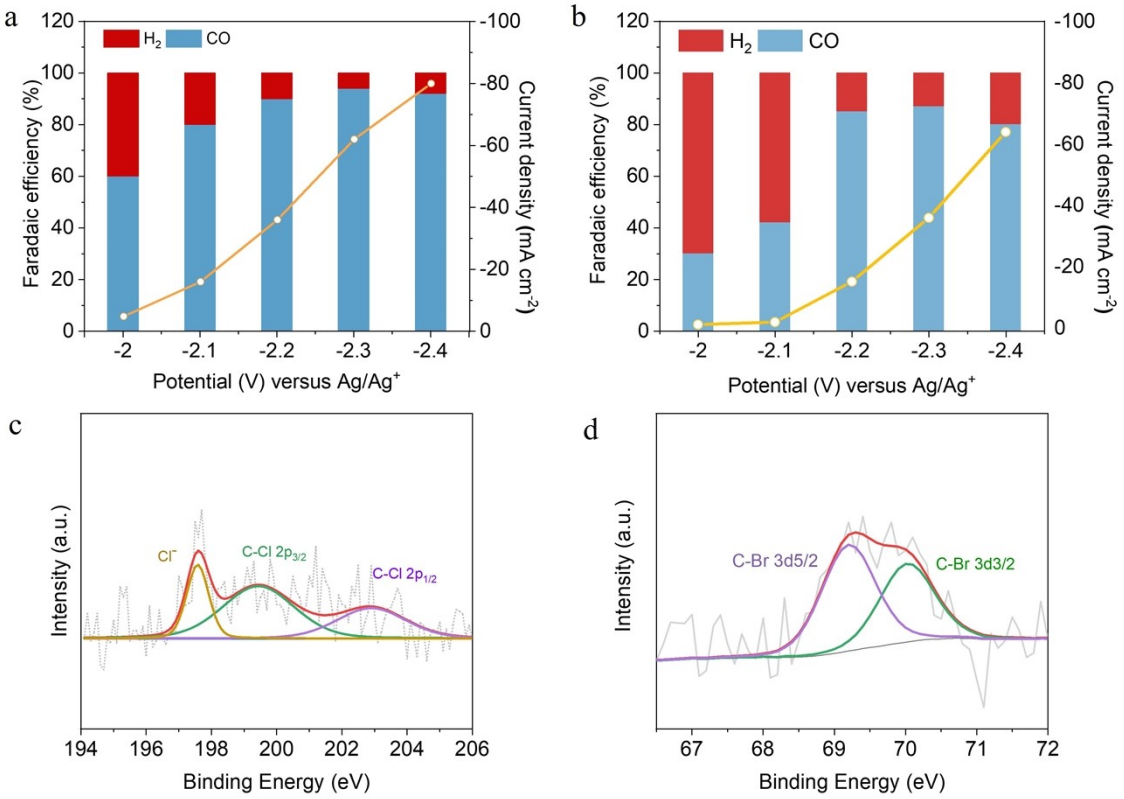

Figure S7. (a) FE of CO and H_2 and the corresponding J_{CO} for CP electrode in BMMImCl/MeCN/H_2O. (b) FE of CO and H_2 and the corresponding J_{CO} for CP electrode in BMMImBr/MeCN/H_2O. (c) Cl 2p spectra of CP_{Cl}. (d) Br 3d spectra of CP_{Br}.

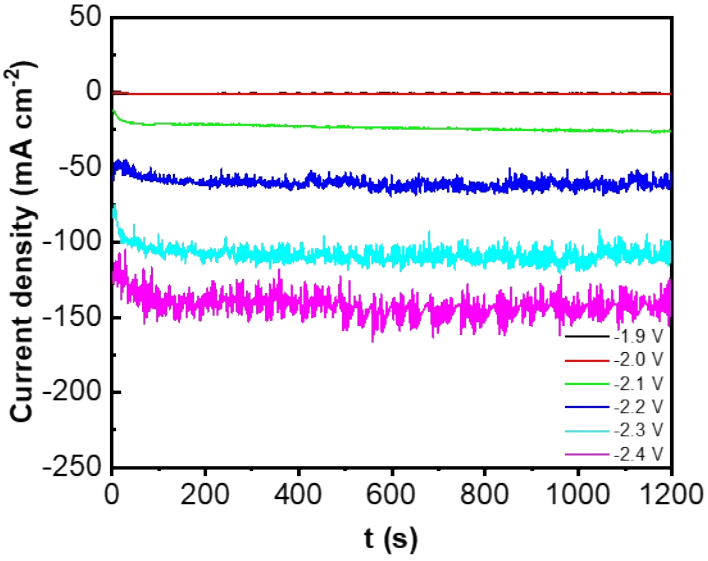

Figure S8. I-t curves for CRR of CP electrode in $BMMImPF_6$/MeCN/H_2O(5wt%) at different potentials.

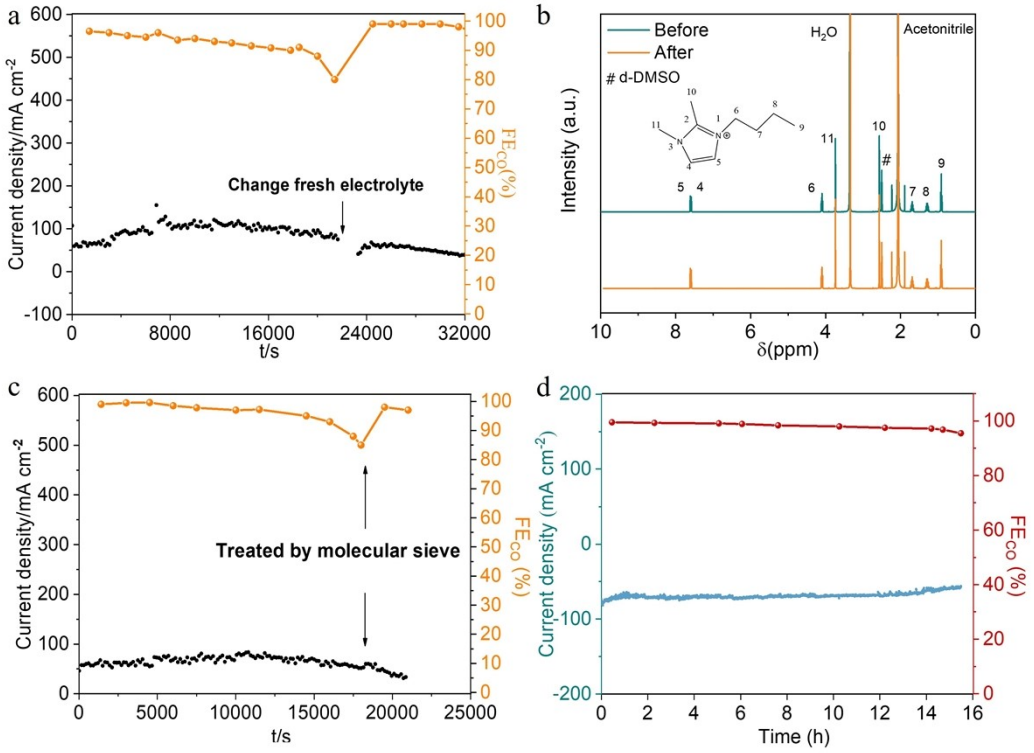

Figure S9. (a) Long-term stability test before and after changing fresh electrolytes in the cell with Nafion exchange membrane. (b) ^{1}H-NMR spectra for the BMMImPF_6/MeCN/H_2O before and after 5 hours electrolysis. (c) Long-term stability test before and after treatment by a molecular sieve in the cell with Nafion exchange membrane. (d) Long-term stability test in the cell with BPM.

In the beginning, the chosen membrane was the Nafion proton exchange membrane, widely employed for segregating the catholyte and anolyte. However, during the extended stability assessment in this system, the catalytic performance of CP decreased significantly after 20000 s electrolysis **(Figure S9a)**. The CO faradaic efficiency decreased from 96.5% to only 80% at 21400 s.

In order to investigate the reasons for such poor stability, we conducted some control experiments. Firstly, after replacing the electrolyte after 21400 s electrolysis, an immediate increase in CO faradaic efficiency from 80% to 99% was observed. This indicates that the active sites of CP retained high catalytic activity after 20000 s. Therefore, we hypothesized that variations in electrolyte composition affected the catalytic stability of this electrochemical system. Then we analyzed NMR spectra of electrolytes before and after long-term electrolysis **(Figure S9b)**, there was no significant change in the peaks of ILs and acetonitrile, indicating no degradation of these components happened after electrolysis.

Since the substantial impact of water content on catalytic performance in non-aqueous systems, Karl Fischer titrations were performed to measure the variation in water content. Surprisingly, the water content increased from approximately 775 ppm to 66839 ppm after 20000 s electrolysis. The increased water content would accelerate the hydrogen evolution process, particularly when surpassing 5 wt%, as previously discussed in the main text. Thus, we proposed that the failure of the long-term stability test was attributable to the continuous increase in water content in the catholyte. To further verify our point, electrolytes after testing were treated with a molecular sieve for an hour, resulting in an immediate recovery of high CO faradaic efficiency **(Figure S9c)**.

Next, we tried to figure out the origin of the increasing water in catholytes. Bubbling the electrolyte with CO_2 gas in a single cell for 20000 s resulted in a slight increase in water content from 423 ppm to 3800 ppm. In contrast, electrolysis in an H-cell with 0.5 M H_2SO_4 as the anolyte for 20000 s led to a dramatic rise in water content from 423 ppm to 50740 ppm, indicating a substantial transfer of water from the anolyte compartment to the catholyte side through the Nafion membrane. As we know, the Nafion proton exchange membrane, manufactured by Dupont, is a perfluoro sulfonic acid (PFSA)-based membrane with sulfonic acid groups immobilized on the polymer backbones. During the

migration of protons through the membrane, water molecules accompany the protons and form H_3O^+ through the membrane from the anode to the cathode due to an electric field effect. Thus, during electrolysis, large amounts of water molecules would migrate from the anolyte to the catholyte, accelerating the competing hydrogen evolution through the Nafion membrane.

To address this challenge, we turned our attention to the bipolar membrane (BPM), comprising a cation exchange layer, an anion exchange layer, and an interfacial layer. Under reverse bias, the water dissociation occurs rapidly in the interfacial layer, transferring H^+ to the CEM side while the hydroxide ions toward the AEM side. By positioning the CEM side facing the cathode, the migration of protons occurs without dragging additional water molecules. Using the BPM for CO_2 reduction in our system, the CP electrode demonstrated significantly improved long-term stability, lasting nearly 15 hours before deactivation, compared to only 5 hours in the Nafion membrane-involved system (**Figure S9d**).

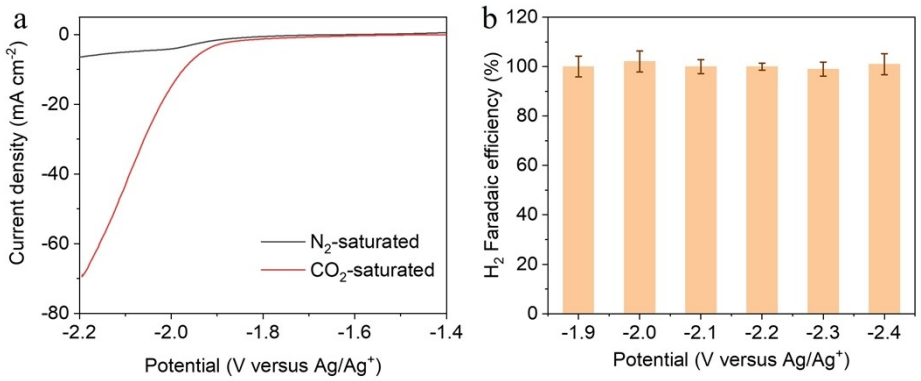

Figure S10. Electrochemical CO_2RR performance of CP in N_2-saturated $BMMImPF_6$/MeCN/H_2O(5wt%). (a) LSV curves, (b) H_2 Faradaic efficiency in the potential range of -1.9 V to -2.4 V vs. Ag/Ag^+.

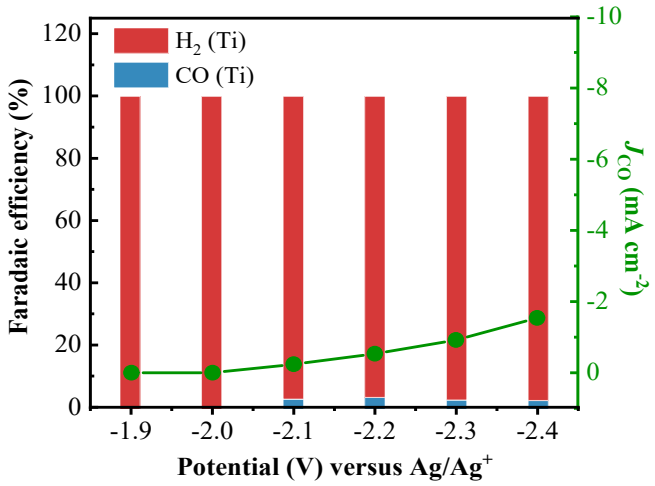

Figure S11. Electrochemical CRR performance of Ti paper in $BMMImPF_6$/MeCN/H_2O electrolyte.

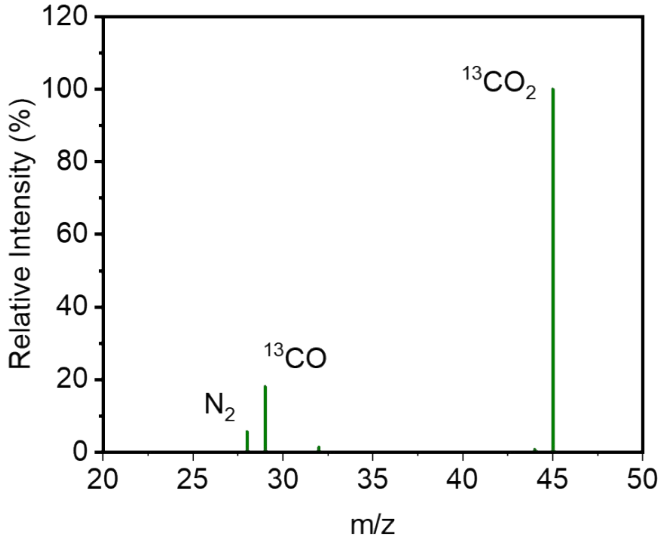

Figure S12. The mass-spectrum of the CRR products using $^{13}CO_2$ as the reactant.

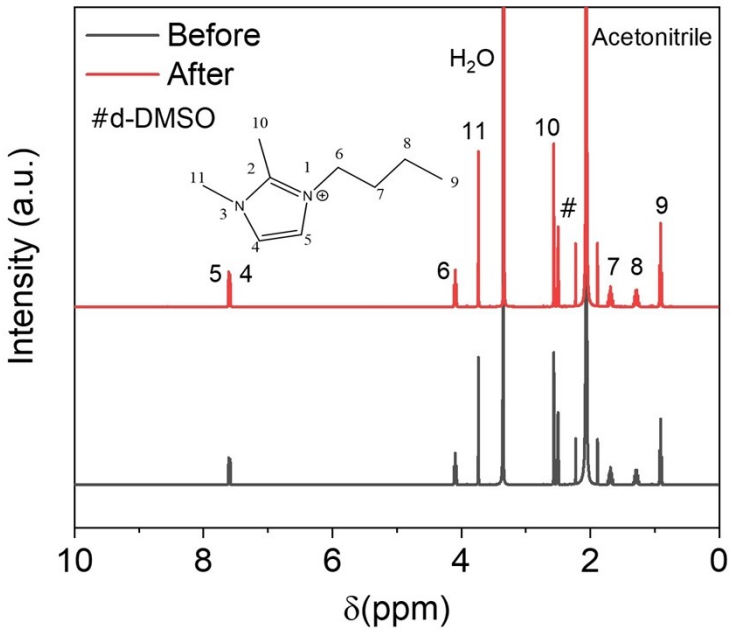

Figure S13. ^{1}H-NMR spectra for the BMMImPF$_6$/MeCN/H$_2$O before and after 15 hours electrolysis.

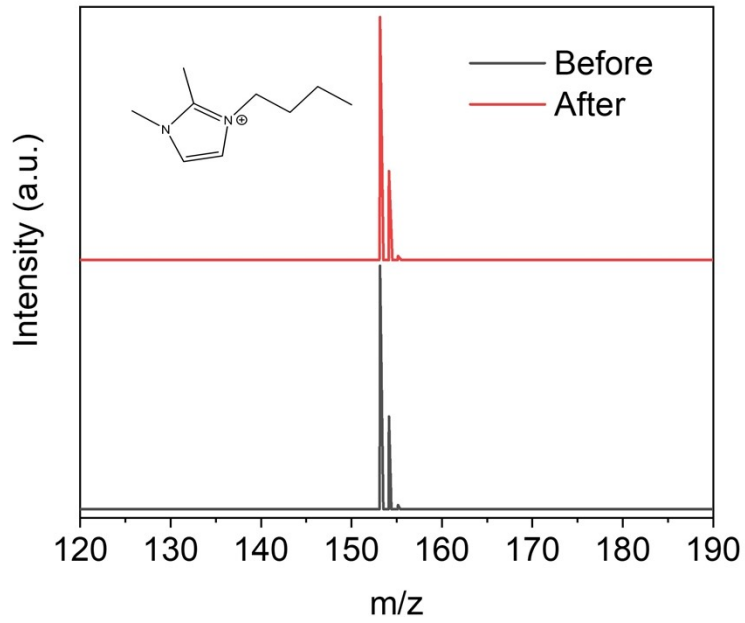

Figure S14. HR-MS spectra for the BMMImPF$_6$/MeCN/H$_2$O before and after 15 hours of electrolysis.

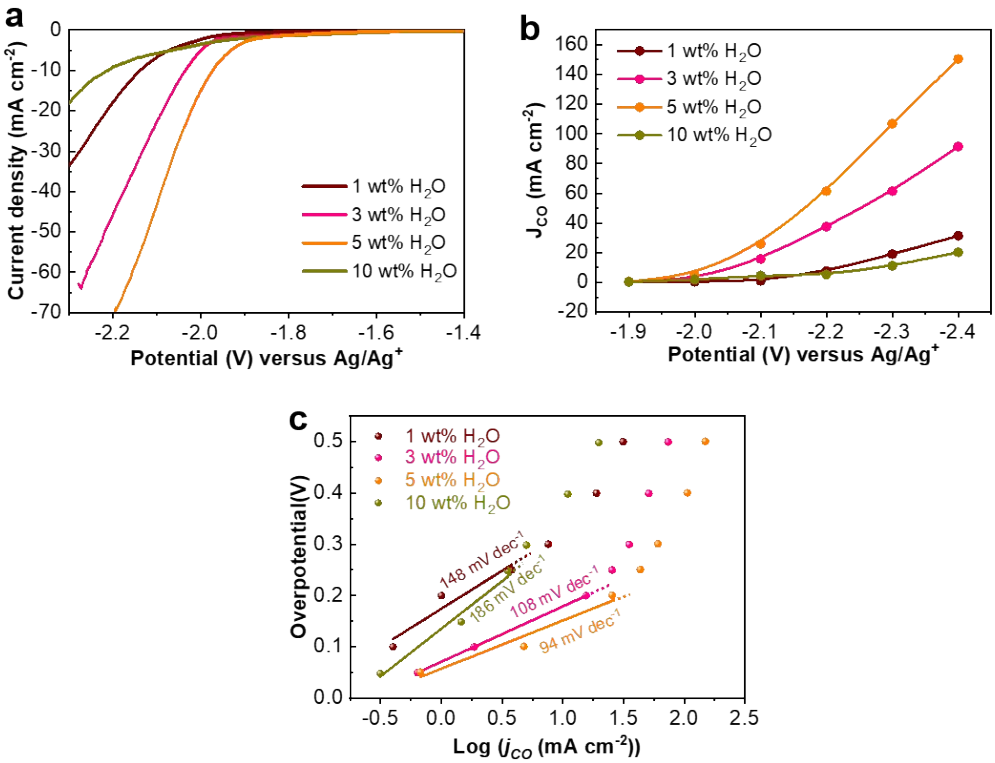

Figure S15. Electrochemical performance of CP using $BMMImPF_6$/AcN/H_2O electrolytes with different content of H_2O. (a) LSV curves at a scan rate of 10 mV/s. (b) Partial current density of CO. (c) Tafel plots and slopes for CP with different H_2O mass ratios.

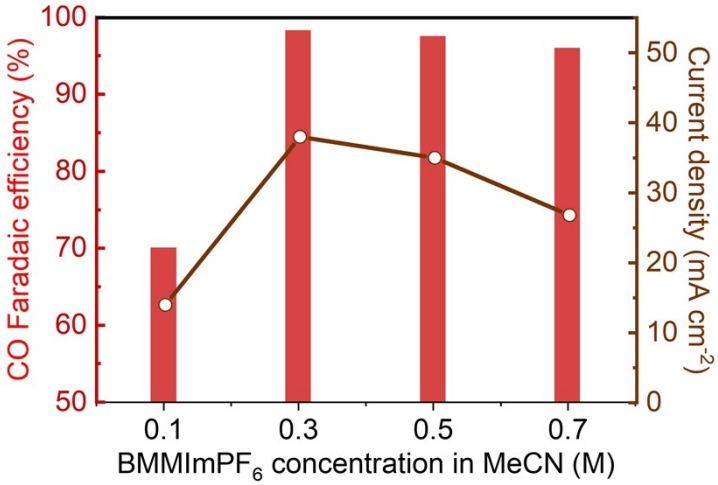

Figure S16. The CO Faradaic efficiency and the current density of CP in electrolytes with varying $BMMImPF_6$ concentration.

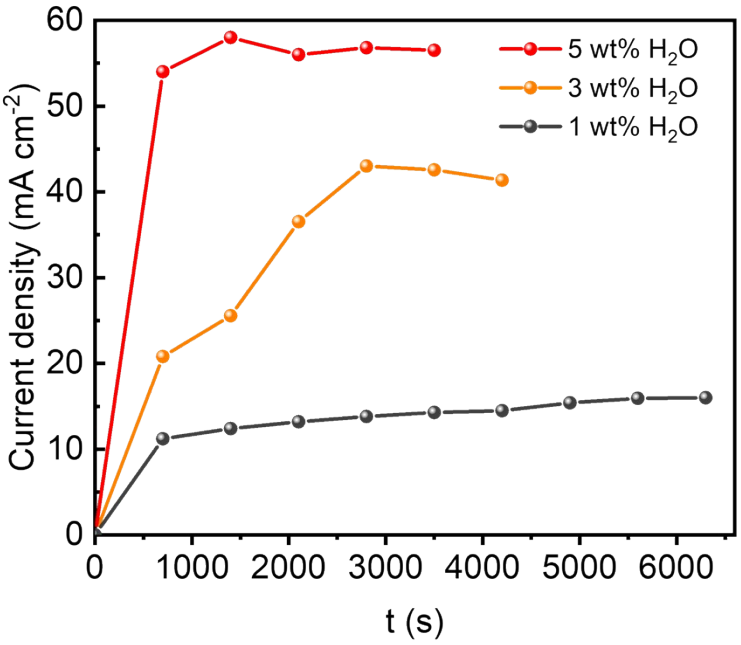

Figure S17. The variation of current density in $BMMImPF_6$/MeCN/H_2O system.

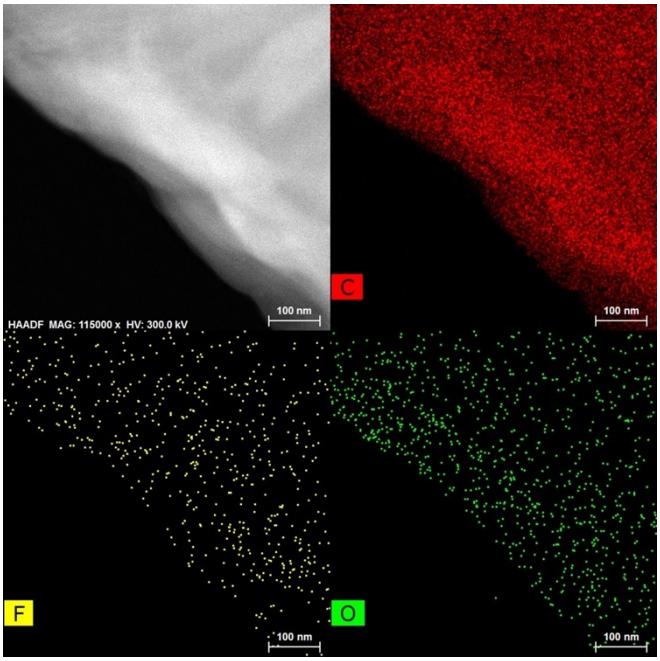

Figure S18. EDS images (C, O, and F atoms) of CP_{PF6}.

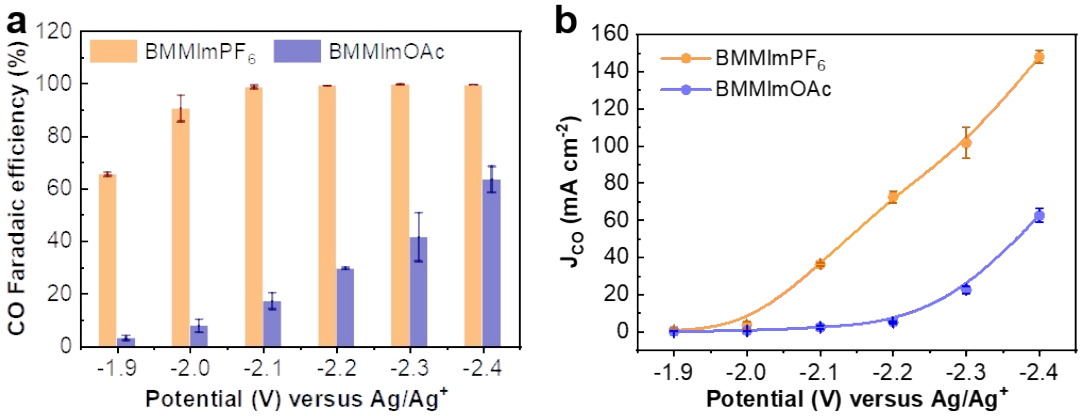

Figure S19. Electrochemical CRR performance of CP in electrolyte with different anions. (a) FE_{CO}, and (b) J_{CO} of CP in BMMImOAc-based and $BMMImPF_6$-based electrolyte.

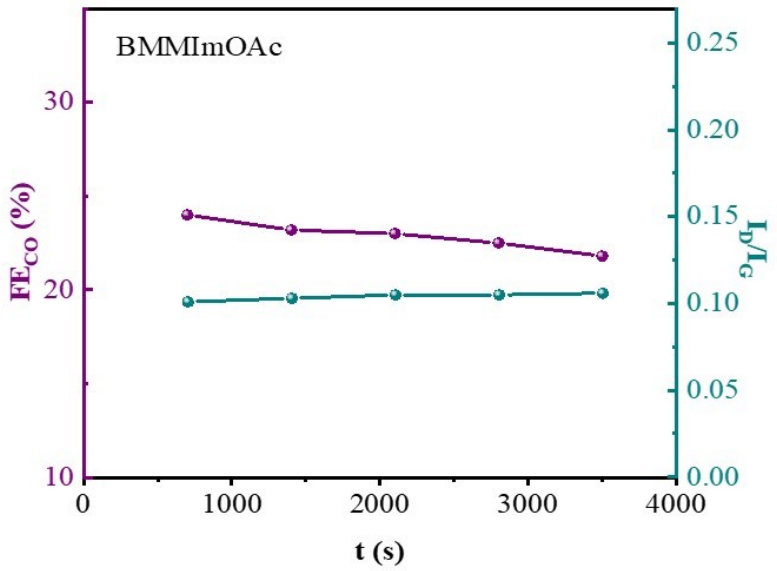

Figure S20. The variation of FE_{CO} and I_D/I_G of CP electrode along with the electrolysis in BMMImOAc based electrolyte at -2.15 V.

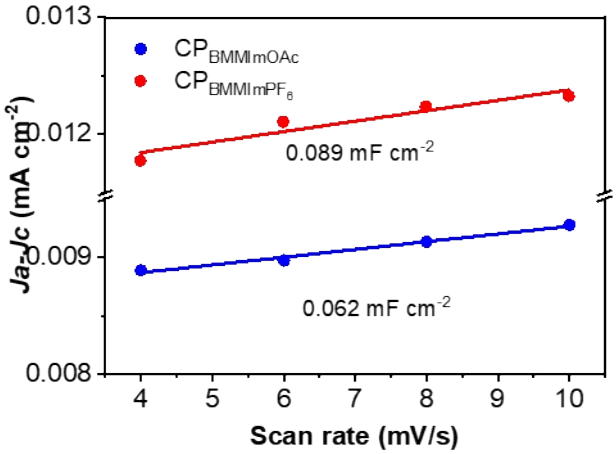

Figure S21. Electrochemically active surface areas estimated from the double-layer capacitance of CP_{OAc} and CP_{PF6}.

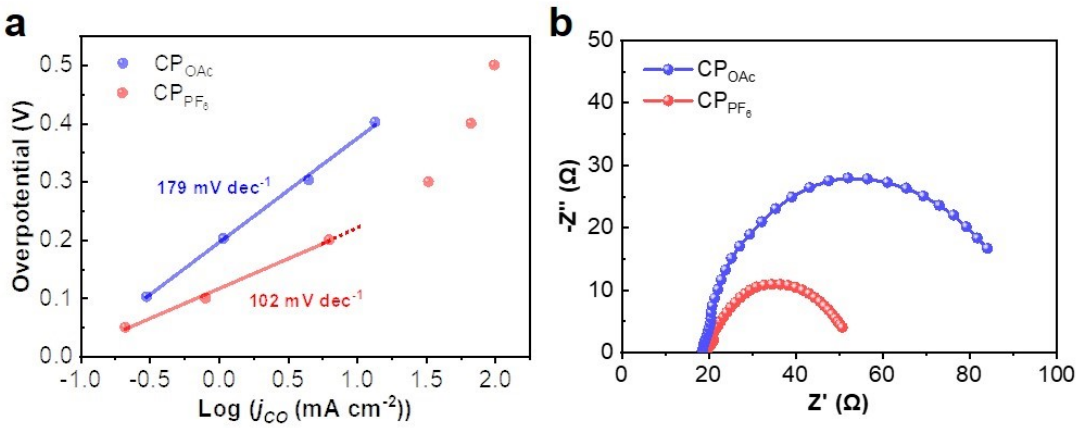

Figure S22. (a) Tafel slops of CP_{OAc} and CP_{PF6}, (b) Nyquist plots of CP_{OAc} and CP_{PF6}.

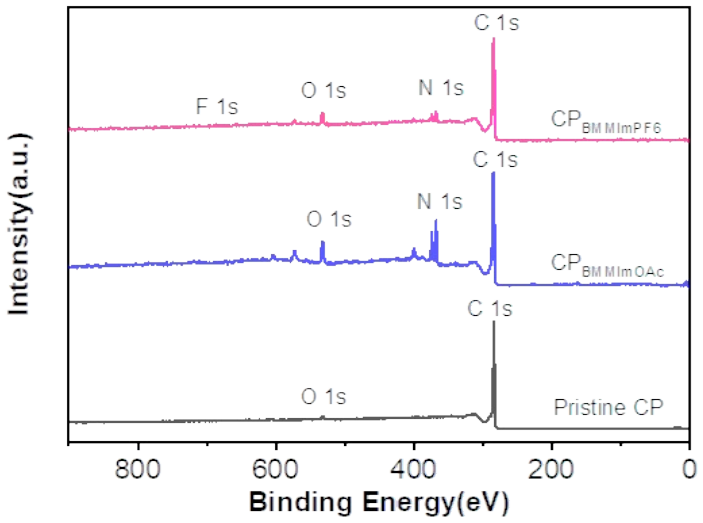

Figure S23. XPS survey spectra of pristine CP, CP_{OAc} and CP_{PF6}.

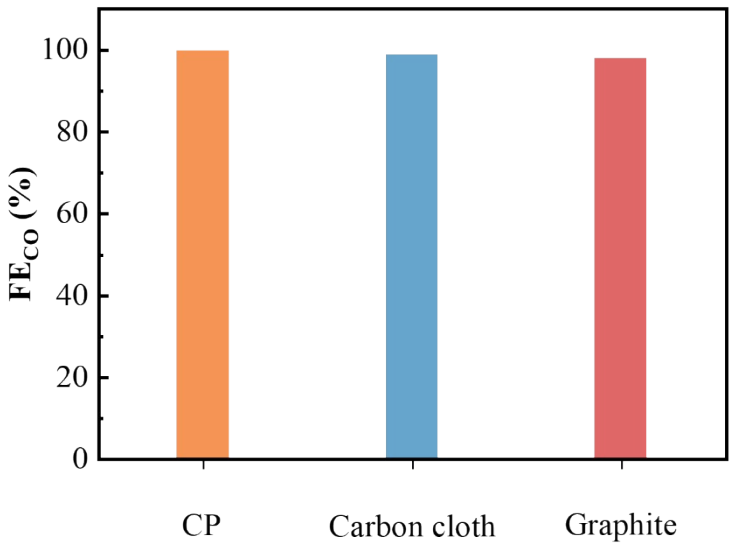

Figure S24. FE_{CO} of CP, carbon cloth and graphite plate at -2.3 V in $BMMImPF_6$/MeCN/H_2O.

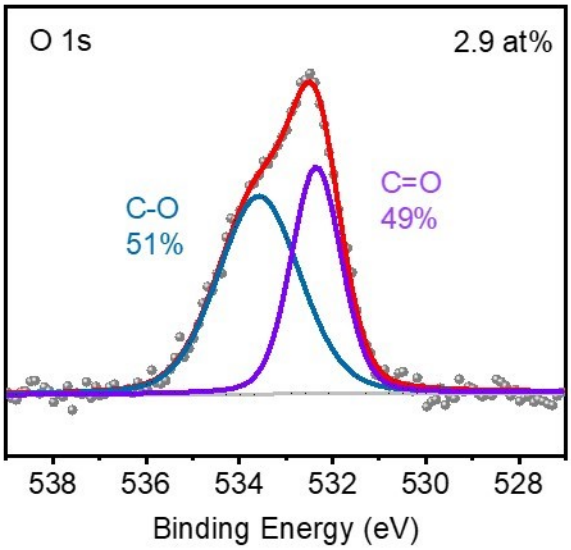

Figure S25. High-resolution XPS O 1s spectrum of pristine CP electrode.

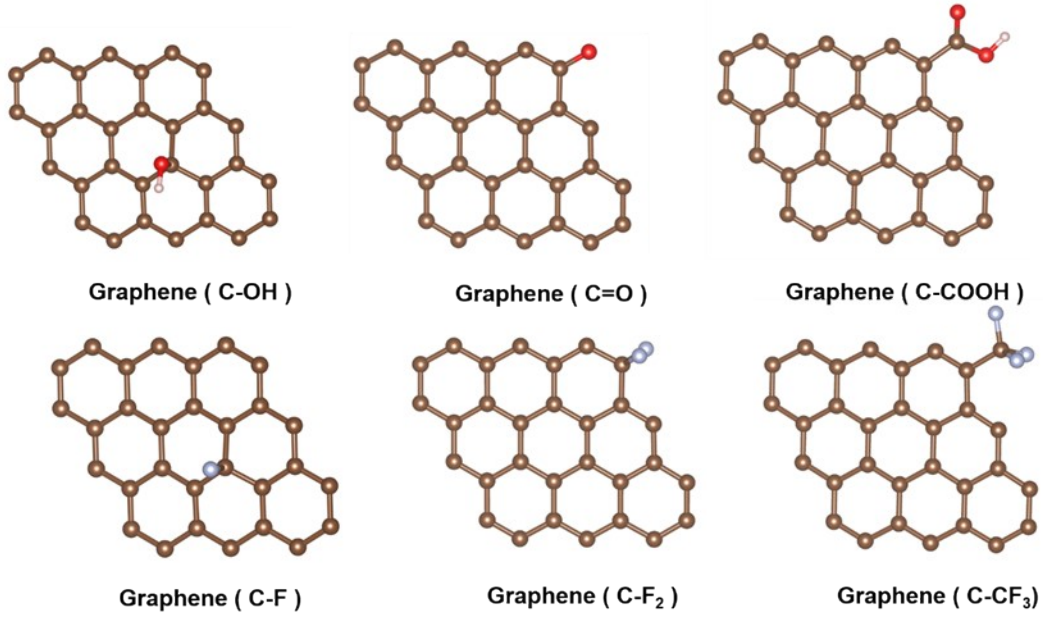

Figure S26. The models for the calculation of the fluoridation substitution process.

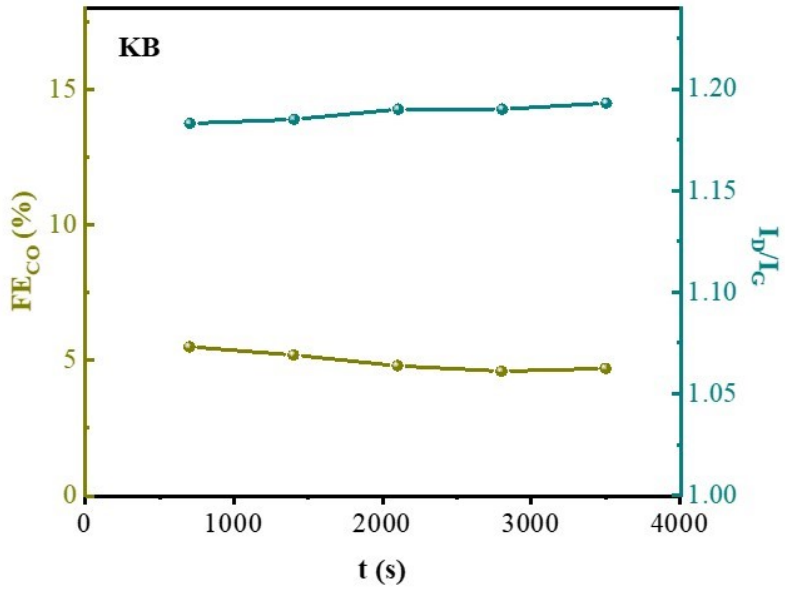

Figure S27. The variation of FE_{CO} and I_D/I_G of KB electrode after electrolysis with different times in $BMMImPF_6$/MeCN/H_2O.

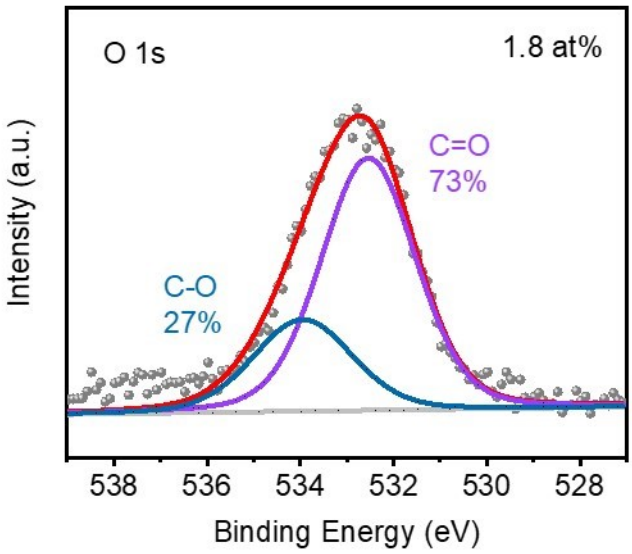

Figure S28. High-resolution XPS O 1s spectrum of pristine KB.

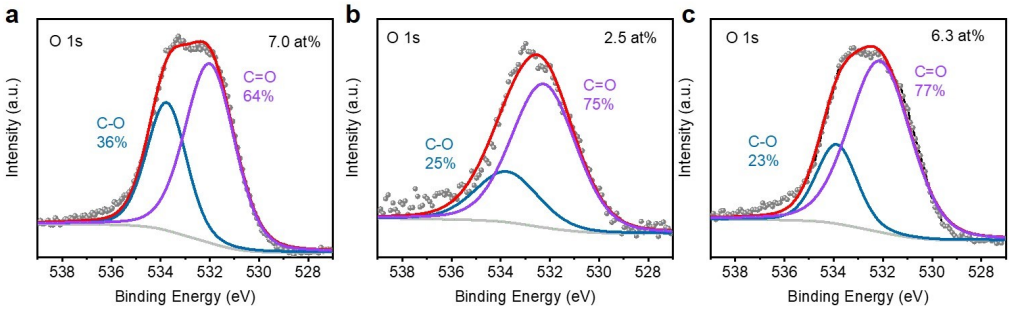

Figure S29. High-resolution XPS O 1s spectrum of (a) $KB_{Acid\text{-}treated}$, (b) $KB_{Air\text{-}450,}$ and (c) $KB_{Air\text{-}600}$.

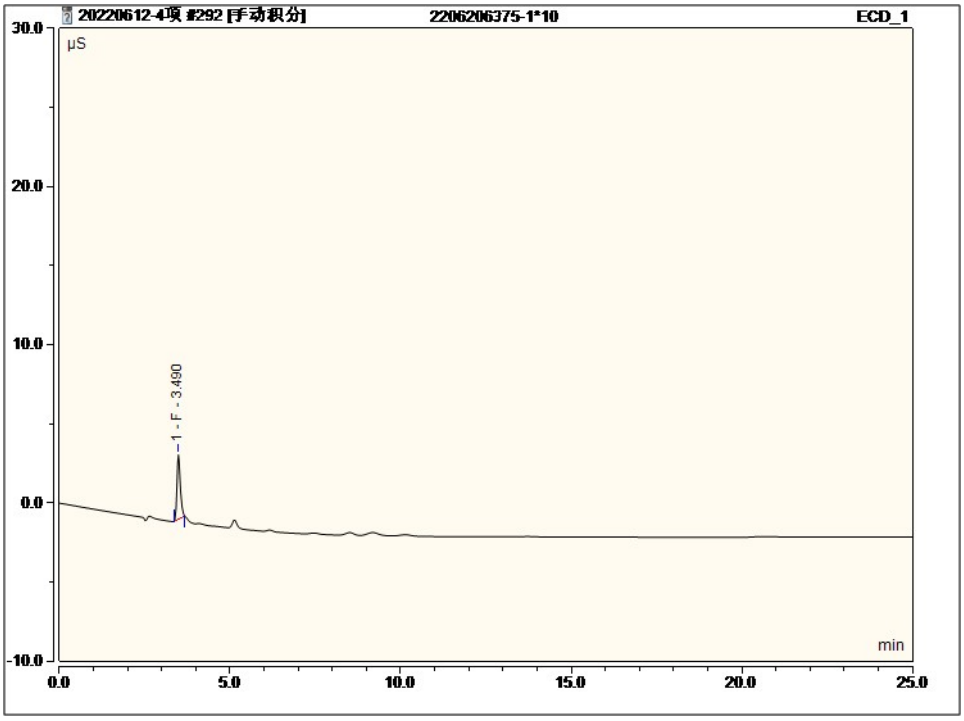

Figure S30. The ion chromatography of $BMMImPF_6$/MeCN/H_2O system.

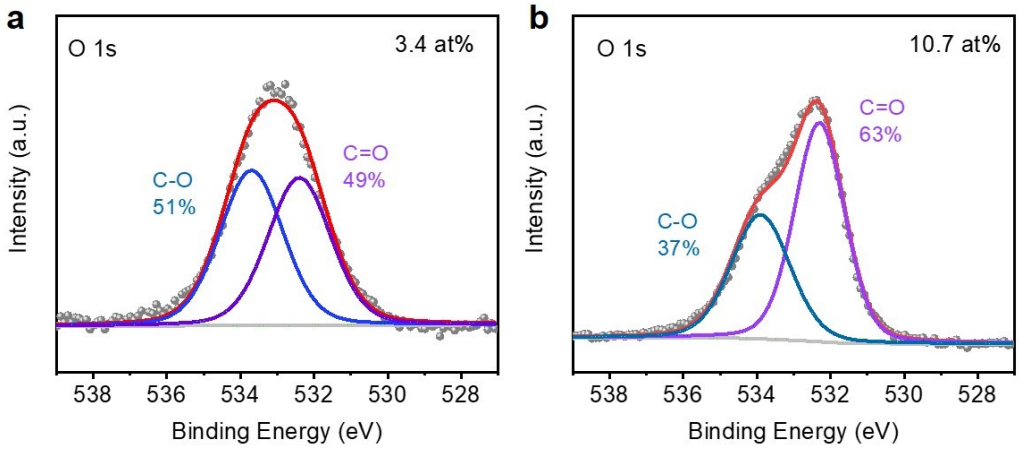

Figure S31. High-resolution XPS O 1s spectrum of (a) Graphite and (b) Carbon cloth.

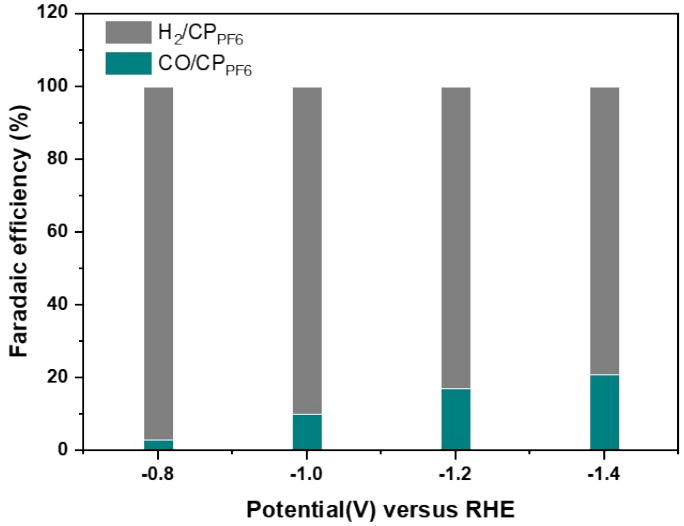

Figure S32. FE of H_2 and CO for CP electrode suffered from activation in $BMMImPF_6$/MeCN/H_2O(5wt%) in 0.1 M $KHCO_3$.

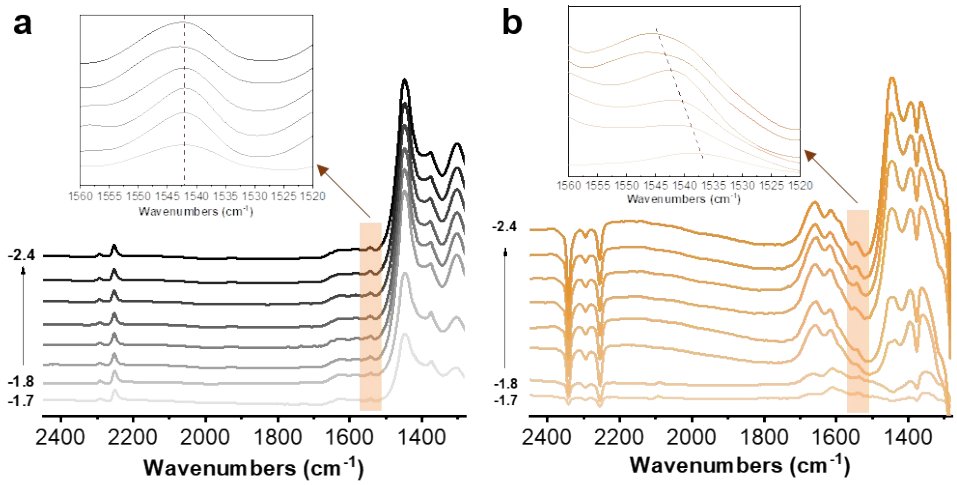

Figure S33. (a) In situ ATR-IR spectra on CP at different cathodic potential using (a) N_2-saturated $BMMImPF_6$/MeCN/H_2O. (b) CO_2-saturated $BMMImPF_6$/MeCN/H_2O.

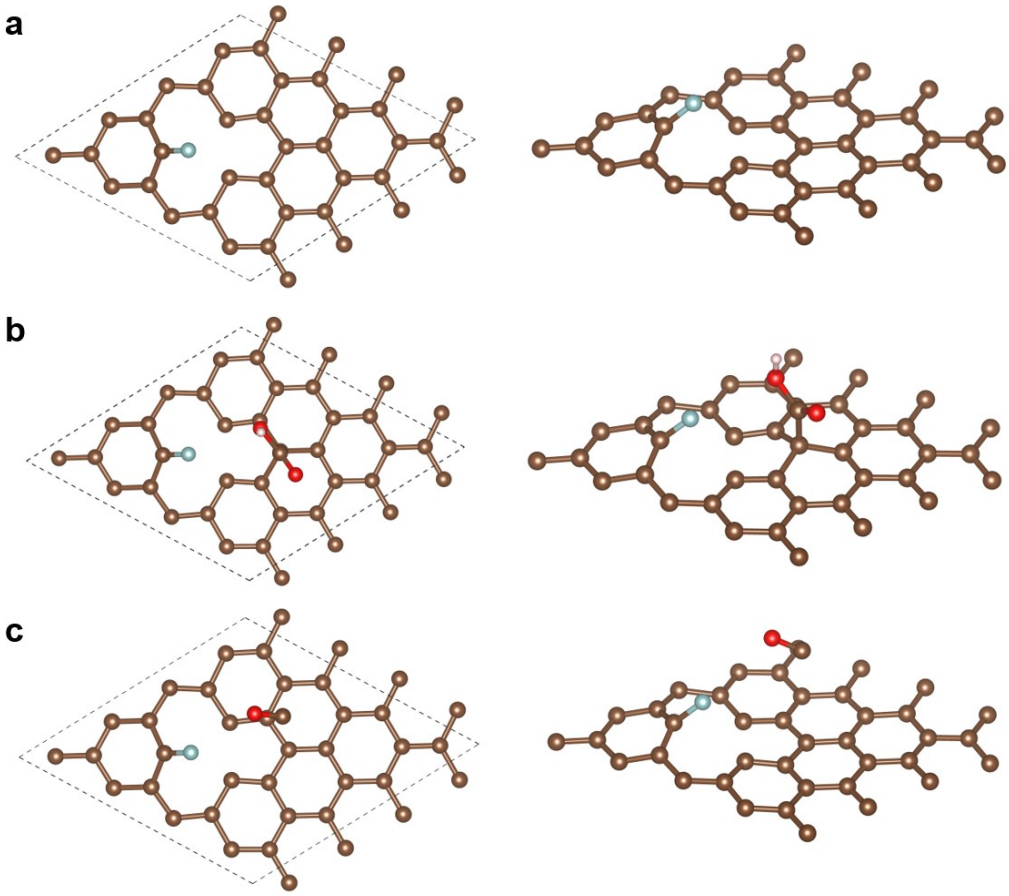

Figure S34. The calculated models for the CRR over F-doped carbon. (a) The pristine F-carbon. (b) The adsorbed *COOH intermediate. (c) The adsorbed *CO.

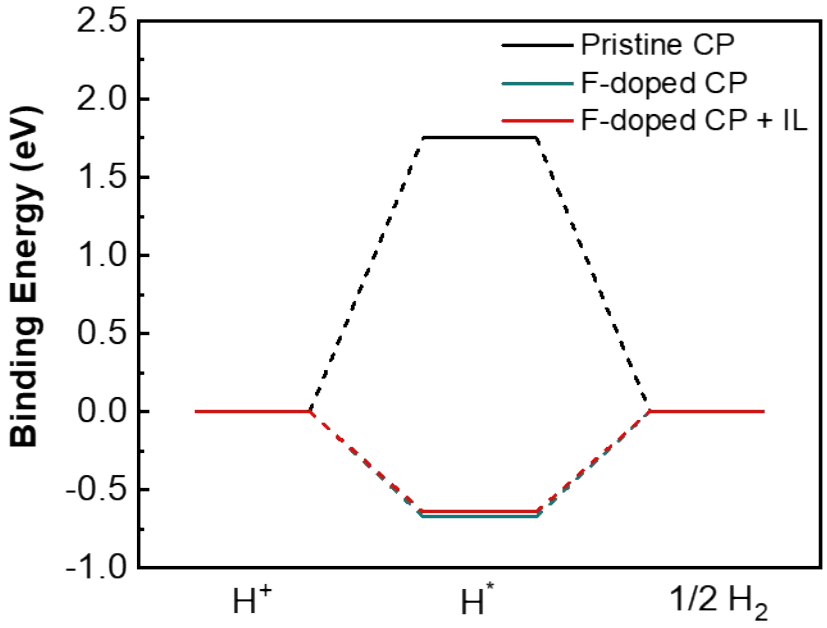

Figure S35. The free energy changes for HER over pristine and F-doped CP, as well as the F-doped CP coupled IL system.

Table S1. Details for the carbon paper used.

Properties	TGP-H-060
Thickness	0.19 mm
Bulk density	0.44 g/cm^3
Porosity	78%
Roughness	8 μm
Gas permeability	1900 mL·mm/[cm^2·hr·mmAq]
Electrical resistivity (through plane)	80 mΩ.cm
Electrical resistivity (in plane)	5.8 mΩ.cm
Flexural strength	40 MPa
Tensile strength	50 N/cm

Table S2. The CRR performance of CP-supported catalysts in both aqueous and non-aqueous electrolytes.

Sample	Electrolyte	FE_{CO}	J_{CO}	Ref.
In_A/NC	0.5 M [Bmim]PF_6/MeCN	97.2%	39.4 mA cm^{-2}	J. Am. Chem. Soc. 2021, 143, 6877−6885
ZnO(OH)/CP-600	([Bmim]PF_6/acetonitrile/H_2O (5 wt%)	97.8%	44.3 mA cm^{-2}	ChemCatChem 2021, 13, 2570–6.
GO/MWCNT-CP	[Bmim]BF_4(90wt%)/ acetonitrile	85%	2.3 mA cm^{-2}	Science China Chemistry 2016, 59 (5), 551-556
In_2Se_3/CP	([Bmim]PF_6 /65wt%acetonitrile/5 wt% H_2O	96.5%	55.3 mA cm^{-2}	Angew.Chem. 2020, 132,2374 –2379
Pd_xBi/CP	[Bmim]PF_6(30wt.%) /acetonitrile(65 wt.%)/H_2O (5 wt.%)	87.7%	7.1 mA cm^{-2}	Chem.Eur. J.2023,29,e20230
DrGO-CoPc/CP	[Bmim]PF_6（30 wt%)/acetonitrile/H_2 O (5 wt%)	93.1%	122 mA cm^{-2}	ACS Appl. Mater. Interfaces 2021, 13, 21, 25523–25532
$Cd(OH)_2$/CP	0.5 M [BMIM]PF_6/MeCN	99%	59 mA cm^{-2}	Chem. Commun., 2018, 54, 5450-5453

PdMo CNSs/CP	0.5 M $[Bmim]PF_6$/MeCN	87.3%	35 mA cm^{-2}	Cell Reports Physical Science 2021, 2 (11).
Co-NB-2/CP	0.5 M $[Bmim]PF_6$/MeCN	97.9%	18.8 mA cm^{-2}	Green Chem., 2022, 24, 1488-1493
OV-rich Bi_2WO_6/CP	0.5 M $[Bmim]PF_6$/MeCN	91%	43 mA cm^{-2}	Green Chemistry 2019, 21 (10), 2589-2593
CdN_4S_1/CN/CP	0.5 M $[Bmim]PF_6$/MeCN	99.7%	182.2 mA cm^{-2}	Angew. Chem. Int. Ed. 10.1002/anie.202105263
DNG-SAFe/CP	0.1 M $KHCO_3$	90%	33 mA cm^{-2}	Adv. Mater. 2020, 2003238
Ni_2-NCNT/CP	0.5 M $KHCO_3$	97%	76 mA cm^{-2}	Applied Catalysis B: Environmental 250 (2019) 347–354
ZnCoNC/CP	0.5 M $KHCO_3$	93.2%	26 mA cm^{-2}	Angew. Chem. Int. Ed.2020,59, 12664–12
FNC-SnOF/CP	0.1 M $KHCO_3$	95.2%	17 mA cm^{-2}	ACS Catal. 2021, 11, 5212−5221
Fe-NS-C/CP	0.1 M $KHCO_3$	98%	7.1 mA cm^{-2}	Nano Energy 68 (2020) 104384

Table S3. Comparisons of the maximum FE_{CO} and J_{CO} of metal-free carbon materials in H-type cell.

Sample	Electrolyte	FE_{CO}	J_{CO}	Ref.
F-CPC	0.5 M $KHCO_3$	88.3%	37.5 mA cm^{-2}	ACS Nano 2020, 14, 2014−2023
FC	0.5 M $KHCO_3$	90%	0.23 mA cm^{-2}	Angew. Chem. Int. Ed. 2018, 57,9640 – 9644
CN-H-	0.1 M $KHCO_3$	88%	0.2 mA cm^{-2}	Adv. Energy Mater.

CNTs				2017, 1701456
NPC-1000	0.5 M $KHCO_3$	98.4%	3.01 mA cm^{-2}	Angew. Chem. Int. Ed. 2020, 59,3244 – 3251
NCNT-NH_3	0.5M $NaHCO_3$	98.6%	26 mA cm^{-2}	Applied Catalysis B: Environmental 250 (2019) 347–354
NG	0.1 M $KHCO_3$	85%	0.8 mA cm^{-2}	Nano Lett. 2016, 16, 466−470
NS-C	0.1 M $KHCO_3$	92%	2.63 mA cm^{-2}	Applied Catalysis B: Environmental 252 (2019) 240–249
NSHCF900	0.1 M $KHCO_3$	94%	103 mA cm^{-2}	Angew.Chem.2018,130,15702–15706
BNMC-1000	0.1 M KHCO3	95%	2.7 mA cm^{-2}	Applied Catalysis B: Environmental 298 (2021) 120543
DPC-NH_3	0.1 M $KHCO_3$	95.2%	2.84 mA cm^{-2}	Adv. Mater. 2020, 2001300
D-NC-1100	0.1 M $KHCO_3$	94.5%	1.5 mA cm^{-2}	Adv. Mater. 2019, 1808276
NRMC	0.1 M $KHCO_3$	80%	2.9 mA cm^{-2}	ACS Energy Lett. 2018, 3, 2292−2298
N,P-carbon	$BMImPF_6$/MeCN/H_2O	99%	143.6 mA cm^{-2}	Angew.Chem.2020,132,11216–11222
CP	$BMMImPF_6$/MeCN/H_2O	~100%	150 mA cm^{-2}	Our work

Table S4. The content of C, O, N and F element in pristine CP, CP_{PF6} and CP_{OAc} detected by XPS.

	C at%	O at%	N at%	F at%
CP	97.43	1.9	/	/
CP_{PF6}	91.06	6.22	1.4	0.60
CP_{OAc}	87.54	7.67	4.4	/

References

1. Kresse, G.; Hafner, J. Ab-initio Molecular-Dynamics Simulation of the Liquid-Metal–Amorphous-Semiconductor Transition in Germanium. Phys. Rev. B 1994, 49 (20), 14251-14269.
2. Kresse, G.; Furthmüller, J. Efficient Iterative Schemes for Ab-initio Total-Energy Calculations using a Plane-Wave Basis Set. Phys. Rev. B 1996, 54 (16), 11169-11186.
3. Blöchl, P. E. Projector Augmented-Wave Method. Phys. Rev. B 1994, 50 (24), 17953-17979.
4. Kresse, G.; Joubert, D. From Ultrasoft Pseudopotentials to the Projector Augmented-Wave Method. Phys. Rev. B 1999, 59 (3), 1758-1775.
5. Hammer, B.; Hansen, L. B.; Nørskov, J. K. Improved Adsorption Energetics within Density-Functional Theory Using Revised Perdew-Burke-Ernzerhof Functionals. Phys. Rev. B 1999, 59 (11), 7413-7421.
6. Monkhorst, H. J.; Pack, J. D. Special Points for Brillouin-Zone Integrations. Phys. Rev. B 1976, 13 (12), 5188-5192.